POLITECNICO DI TORINO
Repository ISTITUZIONALE

Hierarchical Divergence Conforming Bases for Tip Singularities in Quadrilateral Cells

Original
Hierarchical Divergence Conforming Bases for Tip Singularities in Quadrilateral Cells / Graglia, R.D., Peterson, A.F., Petrini, P.. - In: IEEE TRANSACTIONS ON ANTENNAS AND PROPAGATION. - ISSN 0018-926X. - ELETTRONICO. - 68:12(2020), pp. 7986-7994. [10.1109/TAP.2020.3026900]

Availability:
This version is available at: 11583/2858629 since: 2020-12-22T14:07:40Z

Publisher:
IEEE

Published
DOI:10.1109/TAP.2020.3026900

Terms of use:

This article is made available under terms and conditions as specified in the corresponding bibliographic description in the repository

Publisher copyright

(Article begins on next page)

21 June 2026

Hierarchical Divergence Conforming Bases for Tip Singularities in Quadrilateral Cells

Roberto D. Graglia, *Fellow, IEEE*, Andrew F. Peterson, *Fellow, IEEE*, and Paolo Petrini, *Member, IEEE*

***Abstract*— Electromagnetic scattering from targets such as thin conducting plates induce singular currents and charges at sharp edges and sharp tips. In this article, a hierarchical family of divergence-conforming singular basis functions are presented for modeling the singularities associated with current and charge density at tips. These new basis functions are used to increment existing edge-singular bases so that on cells that contain a singular tip where two singular edges join together, the final base combines a hierarchical polynomial representation with linearly independent singular terms that incorporate general exponents that may be adjusted for the specific wedge angle of interest and for the specific angle at the tip. Several variations on the tip functions are proposed.**

***Index Terms*— Basis functions, hierarchical basis functions, method of moments, singular basis functions, tips, wedges.**

I. INTRODUCTION

THE electromagnetic modeling of complex 3-D structures requires numerical techniques. In recent years, higher-order representations have been developed to improve accuracy and efficiency of these approaches [1]. Higher-order representations on smooth parts of an object can be effective, but the presence of wedges, sharp edges, and tips can negate the improvement in efficiency due to the unbounded nature of current and charge densities in these locations. Several types of special basis functions have been developed for the purpose of representing singular currents and charge densities near edges [1]–[3]. To date, less attention has been directed at the effect of tips [4], such as the tips of a square conducting plate [5]. The current density and charge density at a plate tip are known to be infinite, with a singularity that is different from that arising along the plate edge [6]. Throughout this article we use the term "edge singularity" to describe a singularity occurring along a line segment within the domain, such as the boundary of a conducting plate on which the current is expanded. An edge singularity takes up one side of a cell. A "tip singularity" occurs at a single point in a domain, typically the corner of a cell, and involves a different behavior as explained below (see Fig. 1).

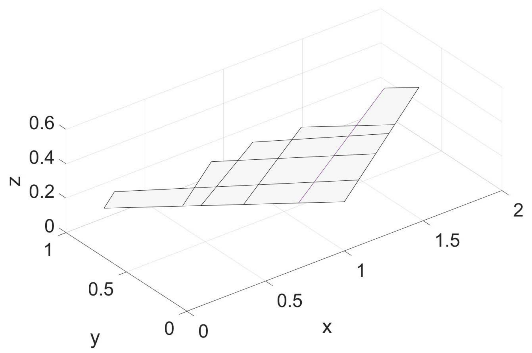

Fig. 1. Flat surface meshed by quadrilateral cells. The surface shown in the figure has 12 edges, eight salient corners, and four reentrant corners. Edge singularities take up one side of a cell; tip singularities occur at a corner of a cell.

A tip singularity may be modeled by the apex of a cone. A conducting cone that has been flattened in the limiting case is known as a plane angular sector (PAS), and can be used to determine the field behavior near the tips of plates or apertures [7]–[9]. The PAS was studied by Satterwhite and Kouyoumjian [7] who proposed an exact solution in sphero-conal coordinates (r, θ, ψ), where r is the distance from the tip and the angle ψ ranges from 0° to 180° across one side of the sector (note that the polar frame (ρ, ϕ) can describe a PAS with a common distance from the tip, but the angles ϕ and ψ are not simply related).

The application of interest is electromagnetic scattering, involving an incident uniform plane wave of monochromatic frequency that induces currents on the conducting target, which in turn produce scattered fields. The PAS scattering problem, just like the canonical problem of the diffraction by a quarter-plane or the scattering from a cone, are classic electromagnetic problems treated by various authors using the Wiener–Hopf or other sophisticated asymptotic techniques (see for example [10]–[22] and references therein). That said, from the exact solution given in [7] one can extract an asymptotic expansion of the current in terms of sphero-conal coordinates [4]

$$J_r \simeq \sum_{n=0}^{\infty} \sum_{q=1}^{\infty} \frac{A_{2n-1,q}(\psi)\, r^{2n-1+\nu_{o,q}} + A_{2n,q}(\psi)\, r^{2n+\nu_{e,q}}}{\sin \psi} \tag{1}$$

Manuscript received March 6, 2020; revised July 23, 2020; accepted August 8, 2020. Date of publication October 1, 2020; date of current version December 17, 2020. This work was supported in part by the Italian Ministry of Education, University and Research (MIUR) through Progetti di Ricerca di Rilevante Interesse Nazionale (PRIN) under Grant 2017NT5W7Z. *(Corresponding author: Roberto D. Graglia.)*

Roberto D. Graglia and Paolo Petrini are with the Dipartimento di Elettronica e Telecomunicazioni, Politecnico di Torino, 10129 Turin, Italy (e-mail: roberto.graglia@polito.it; paolo.petrini@polito.it).

Andrew F. Peterson is with the School of Electrical and Computer Engineering, Georgia Institute of Technology, Atlanta, GA 30332 USA (e-mail: peterson@ece.gatech.edu).

Color versions of one or more figures in this article are available at https://doi.org/10.1109/TAP.2020.3026900.

Digital Object Identifier 10.1109/TAP.2020.3026900

This work is licensed under a Creative Commons Attribution 4.0 License. For more information, see https://creativecommons.org/licenses/by/4.0/

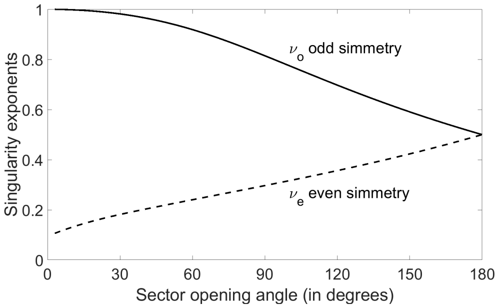

Fig. 2. Singularity exponents for salient PEC sectors.

$$J_\psi \simeq \sin\psi \sum_{n=0}^{\infty}\sum_{q=1}^{\infty} B_{2n-1,q}(\psi)\, r^{2n-1+\nu_{o,q}} \tag{2}$$

with a corresponding expression for the charge density in the form

$$\nabla\cdot\boldsymbol{J} \simeq \sum_{n=0}^{\infty}\sum_{q=1}^{\infty} \frac{C_{2n-1,q}(\psi)\, r^{2n-1+\nu_{e,q}} + C_{2n,q}(\psi)\, r^{2n+\nu_{o,q}}}{\sin\psi}. \tag{3}$$

The exponents in (1)–(3) are the sum of an integer m (even or odd) that depends on the outer summation index n plus an irrational number (indicated by the Greek letter $\nu_{o,q}$ or $\nu_{e,q}$) that depends on the inner summation index q. These exponents do not depend on the frequency and grow slowly with q and more rapidly with n [4]. The so-called even or radial current-components are associated with even values of $m = 2\ n$. The odd or tangential current-components are associated with odd values of $m = 2n - 1$. The even/odd designation originates with the type of boundary conditions imposed on the Lame equations [7]. Note that (2) involves only odd exponents. Note also that the terms in the sums (1)–(3) may or may not be excited from a particular source, and therefore may or may not be present in a particular solution even if a vertex is present.

Brinkley [23] used the results of [7] to improve the accuracy of the far-field results obtained with high-frequency techniques and current-based approaches (i.e., physical optics and its extensions) in many nonspecular regions around a flat plate. In fact, by considering a finite (but not too small) number of coefficients ν_{oq} and ν_{eq}, one gets better approximations of "the diffracted vertex current" that yield results that compare better with numerical results and measurements for most cases.

The tangential current component is unbounded along the two edges forming the tip, although the even components vanish at the tip. Of interest is the fact that the leading order singularity of the current (1), and (2) is not directly related to that of the charge density (3). In fact, (1) and (2) and Fig. 2 show that for salient sectors the leading order singularity of the current is $\nu_o - 1$ while that for the charge density is $\nu_e - 1$.

Throughout this article, as in (1)–(3), we denote terms related to even components with the subscript "e," while we use the subscript "o" to denote terms related to odd components. In the following the dependence on q is understood and the (integer) subscript q may be omitted. In addition, we sometimes specify the singularity order by the values of q and n since in the exponents we report the correct value $2n$ and $2n - 1$ for the even and odd components, respectively.

The critical parameters are the exponents ν_o and ν_e of "salient" perfect electric conducting (PEC) sectors shown in Fig. 2 for $q = 1$; these exponents may be obtained in the manner developed in [7] and have been tabulated in [4] up to $q = 4$ (for a 90° sector), and in [6] and [9] for $q = 1$. Sectors having aperture angle higher than 180° are termed "reentrant"; these are out of the scope of this article and ought to be numerically modeled in a manner different from the one reported in this article.

Previous work on this topic was published by Andersson, who carried out a method of moments (MoM) analysis of the rectangular plate by developing special basis functions that provide the leading order current and charge singularities on rectangular cells within the electric field integral equation (EFIE) [5]. However, most MoM approaches for the EFIE are based on divergence-conforming basis functions, and Andersson's functions for the square plate are only approximately so. A second attempt at the corner problem was proposed by Ozturk *et al.* [24], who employed triangular cells, but included only one exponent at the tip.

In the following, improved divergence-conforming basis functions are proposed for modeling tip singularities of salient sectors of arbitrary aperture angle. These new functions form a hierarchical set whose lowest-order members are motivated by the Andersson bases; members of the set may be added to the edge-singular bases of [3] in cells connected to tips to more properly model the current and charge density singularities. We present results for planar conducting plates.

Section II discusses why numerical models capable of modeling edge singularities are inadequate for modeling tip singularities. Section III introduces the coordinates and variables used to describe tip cells. The new functions to model the odd and even current component near a tip are presented and discussed in Section IV. The functions of Section IV span three rectangular cells; Section V introduces corrective techniques that reduce the domain of the tip singular functions to a single quadrilateral cell. The numerical technique used to compute the MoM integrals associated with singular tip-functions is described in a companion article [25], while [26] describes the integration of the edge-singular basis functions given in [3]. Numerical results in the frequency domain are reported and discussed in Section VI.

II. WHAT THE OTHER HIGH-ORDER BASES ARE MISSING

The inadequacy of polynomial or edge-singular bases to deal with tip singularities is evident by considering the behavior of the current near a 90° sector tip; in this case the leading order singularity of the current is $\nu_o - 1 = -0.18534$ while that of the charge density is $\nu_e - 1 = -0.70342$ (see [4]). For salient sectors the singularity of the charge density of the even current-component is always stronger than that of the odd current-component.

Table I reports the Andersson bases in the Cartesian reference system with origin at the 90° sector tip [5]. The bottom

TABLE I
ODD AND EVEN CURRENT-COMPONENTS FOR A 90° TIP

Andersson's basis functions [5]

$$\nu_o = 0.81466 \qquad 1-\nu_o = 0.18534$$

$$\boldsymbol{J}_o = \frac{1}{\sqrt{(x^2+y^2)^{1-\nu_o}}}\left[\frac{1}{2}\left(\sqrt{\frac{y}{x}}\,\hat{\boldsymbol{y}} - \sqrt{\frac{x}{y}}\,\hat{\boldsymbol{x}}\right) -(1-\nu_o)\sqrt{\frac{x\,y}{x^2+y^2}}\left(\frac{x\,\hat{\boldsymbol{y}}}{\sqrt{x^2+y^2}} - \frac{y\,\hat{\boldsymbol{x}}}{\sqrt{x^2+y^2}}\right)\right]$$

$$\boldsymbol{\nabla}\cdot\boldsymbol{J}_o = 0$$

$$\nu_e = 0.29658 \qquad 1-\nu_e = 0.70342$$

$$\boldsymbol{J}_e = \sqrt{(x^2+y^2)^{\nu_e}}\left(\sqrt{\frac{y}{x}}\,\hat{\boldsymbol{y}} + \sqrt{\frac{x}{y}}\,\hat{\boldsymbol{x}}\right)$$

$$\boldsymbol{\nabla}\cdot\boldsymbol{J}_e = \frac{(1+\nu_e)}{\sqrt{(x^2+y^2)^{1-\nu_e}}}\sqrt{\frac{x^2+y^2}{x\,y}}$$

Approximation of Andersson's basis functions by linear combination of the basis functions [3, Table II]

$$\boldsymbol{J}_{o_{\text{approx.}}} = \frac{y}{\sqrt{x}}\,\hat{\boldsymbol{y}} - \frac{x}{\sqrt{y}}\,\hat{\boldsymbol{x}}$$

$$\boldsymbol{\nabla}\cdot\boldsymbol{J}_{o_{\text{approx.}}} = \frac{1}{2}\left(\frac{1}{\sqrt{x}} - \frac{1}{\sqrt{y}}\right)$$

$$\boldsymbol{J}_{e_{\text{approx.}}} = \frac{y}{\sqrt{x}}\,\hat{\boldsymbol{y}} + \frac{x}{\sqrt{y}}\,\hat{\boldsymbol{x}}$$

$$\boldsymbol{\nabla}\cdot\boldsymbol{J}_{e_{\text{approx.}}} = \frac{1}{2}\sqrt{\frac{(x+y)^2}{x\,y}}$$

of Table I reports the "reconstructed" currents and divergences obtained from the hierarchical basis of [3, Table II] consisting of edge-singular functions associated with the two edges that form the sector tip. The fact that the charge density (3) does not contain a term proportional to r^{ν_o-2} led Andersson to model the "odd" current-component proportional to r^{ν_o-1} with a basis function having zero divergence over its entire definition domain [5].

By rewriting the Andersson bases from Table I in polar (ρ, ϕ) coordinates, one obtains equations that agree with (1)–(3); for instance,

$$\sqrt{\frac{x^2+y^2}{x\,y}} = \frac{1}{\sqrt{\sin\phi\,\cos\phi}} = \frac{\sqrt{2}}{\sqrt{\sin(2\phi)}}. \tag{4}$$

Although the Andersson basis functions and the reconstructed functions of Table I obtained from the hierarchical basis of [3, Table II] look similar, the odd current of Andersson is unbounded at the tip whereas the reconstructed $\boldsymbol{J}_{o_{\text{approx.}}}$ is exactly equal to zero on the sector tip to satisfy the boundary conditions along the edges. Also, the divergence of $\boldsymbol{J}_{o_{\text{approx.}}}$ vanishes for x and y going to zero with the same speed, i.e., for $x = y \to 0$. A similar consideration is repeated for the even current-components. At the tip, the singularity of the divergence of Andersson's function is completely different from the reconstructed one. Approaching the tip, both $\boldsymbol{\nabla}\cdot\boldsymbol{J}_e$ and $\boldsymbol{\nabla}\cdot\boldsymbol{J}_{e_{\text{approx.}}}$ diverge, but clearly with different rates since, from Table I

$$\frac{\boldsymbol{\nabla}\cdot\boldsymbol{J}_e}{\boldsymbol{\nabla}\cdot\boldsymbol{J}_{e_{\text{approx.}}}} = 2\,(1+\nu_e)\,\frac{\sqrt{\left(x^2+y^2\right)^{\nu_e}}}{x+y}. \tag{5}$$

This suggests that the models must be improved in the immediate vicinity of the tip itself. In Sections III–V, we introduce vector sets able to mimic the asymptotic expressions (1)–(3) and then extract basis functions of singularity order q and n. In the end, we will retain only the functions that are unbounded at the tip. This implies that we will retain only the functions with singularity order $n = 0$ because the other functions for $n \geq 1$ yield a zero contribution to the current and its divergence around the tip.

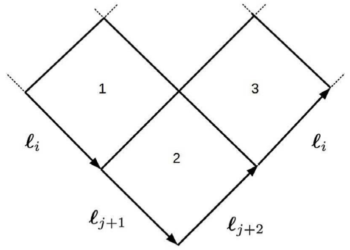

Fig. 3. Tip functions span three adjacent quadrilateral cells, locally numbered counterclockwise from 1 to 3. The tip of the sector coincides with the free vertex of cell 2, not adjacent to cell 1 nor to cell 3. The tip aperture angle of the salient sector is between 0° and 180°.

III. PARENT VARIABLES AND SINGULAR FUNCTIONS ON TIP CELLS

The tip basis functions are piecewise defined on three adjacent quadrilateral cells, locally numbered counterclockwise from 1 to 3 in Fig. 3. The tip of the sector coincides with the free vertex of cell 2, not adjacent to cell 1 nor to cell 3.

Each basis function piece is defined on a 2-D parent-cell, and then mapped onto the 3-D observer or child space. The vector $\boldsymbol{r}$ denotes a point in the child space. In turn, the cells are parametrized by four dummy parent-variables $\left\{\xi_\beta, \xi_{\beta\pm1}, \xi_{\beta+2}\right\}$ whose subscripts are counted modulo 4, with [1]

$$\xi_\beta + \xi_{\beta+2} = 1 \tag{6}$$

$$\xi_{\beta+1} + \xi_{\beta-1} = 1. \tag{7}$$

The cell edges are also locally numbered from 1 to 4 in counterclockwise order, and four edge-vectors that are functions of the child-variable $\boldsymbol{r}$ are then defined, with [1]

$$\boldsymbol{\ell}_\beta + \boldsymbol{\ell}_{\beta\pm2} = 0. \tag{8}$$

To avoid confusion, we identify with different subscripts the variables and the edge-vectors of cell 2 with respect to those used for cells 1 and 3, so as to ensure the following.

1) Cell 1 has its $\xi_{i+1} = 0$ edge in common with the $\xi_j = 0$ edge of cell 2.
2) Cell 3 has its $\xi_{i-1} = 0$ edge in common with the $\xi_{j-1} = 0$ edge of cell 2.

Hence, the dummy variables used to describe cells 1 and 3 are $\{\xi_i, \xi_{i\pm1}, \xi_{i+2}\}$, while cell 2 is described by the variables

TABLE II

ODD AND EVEN FUNCTIONS OF ORDER n, FOR $n \geq 0$ AND INTEGER

<table>
<tr><th>Odd tangential functions</th><th>Even radial functions</th></tr>
<tr><td>$\boldsymbol{T}$ is associated with a single DoF and is piecewise defined on the adjacent cells $q = 1$, 2 and 3, with $\boldsymbol{T} = \boldsymbol{T}_q$ on cell q
$$\boldsymbol{T}_2 = \mathcal{T}_n\left(\xi_{j+1}, \xi_{j+2}\right) \boldsymbol{\Lambda}_j(\boldsymbol{r}) - \mathcal{T}_n\left(\xi_{j+2}, \xi_{j+1}\right) \boldsymbol{\Lambda}_{j-1}(\boldsymbol{r})$$
$$\boldsymbol{\nabla} \cdot \boldsymbol{T}_2 = 0$$
$$\boldsymbol{T}_1 = -\mathcal{T}_n\left(\xi_i, 1\right) \boldsymbol{\Lambda}_{i+1}(\boldsymbol{r}), \quad \boldsymbol{\nabla} \cdot \boldsymbol{T}_1 = -\frac{\mathcal{T}_n\left(\xi_i, 1\right)}{\mathcal{J}}$$
$$\boldsymbol{T}_3 = +\mathcal{T}_n\left(\xi_i, 1\right) \boldsymbol{\Lambda}_{i-1}(\boldsymbol{r}), \quad \boldsymbol{\nabla} \cdot \boldsymbol{T}_3 = +\frac{\mathcal{T}_n\left(\xi_i, 1\right)}{\mathcal{J}}$$</td><td>$\boldsymbol{R}$ is associated with a single DoF and is piecewise defined on the adjacent cells $q = 1$, 2 and 3, with $\boldsymbol{R} = \boldsymbol{R}_q$ on cell q
$$\boldsymbol{R}_2 = \mathcal{R}_n\left(\xi_{j+1}, \xi_{j+2}\right) \left[\boldsymbol{\Lambda}_j(\boldsymbol{r}) + \boldsymbol{\Lambda}_{j-1}(\boldsymbol{r})\right]$$
$$\boldsymbol{\nabla} \cdot \boldsymbol{R}_2 = (2n + \nu_e + 1) \frac{\mathcal{R}_n\left(\xi_{j+1}, \xi_{j+2}\right)}{\mathcal{J}} + (2n + \nu_e - 1) \frac{K_R}{\mathcal{J}}$$
$$\boldsymbol{R}_1 = -\mathcal{R}_n\left(\xi_i, 1\right) \boldsymbol{\Lambda}_{i+1}(\boldsymbol{r}), \quad \boldsymbol{\nabla} \cdot \boldsymbol{R}_1 = -\frac{\mathcal{R}_n\left(\xi_i, 1\right)}{\mathcal{J}}$$
$$\boldsymbol{R}_3 = -\mathcal{R}_n\left(\xi_i, 1\right) \boldsymbol{\Lambda}_{i-1}(\boldsymbol{r}), \quad \boldsymbol{\nabla} \cdot \boldsymbol{R}_3 = -\frac{\mathcal{R}_n\left(\xi_i, 1\right)}{\mathcal{J}}$$</td></tr>
<tr><td colspan="2">$\mathbf{V}_{j+1}$ and $\mathbf{V}_{j+2}$ are bubble functions that span only the number 2 cell. The bubble functions on cells 1 and 3 remain the same as in [3]
$$\mathbf{V}_{j+1} = \sqrt{\xi_{j+1}\, \xi_{j+2}}\, P_n\left(\boldsymbol{\xi}, \nu_o\right) \boldsymbol{\Lambda}_{j+1}(\boldsymbol{r}), \quad \boldsymbol{\nabla} \cdot \mathbf{V}_{j+1} = \sqrt{\frac{\xi_{j+2}}{\xi_{j+1}}} \left[\frac{3\xi_{j+1} - 1}{2} + (2n + \nu_o) \frac{\left(\xi_{j+1} - 1\right) \xi_{j+1}^2}{\xi_{j+1}^2 + \xi_{j+2}^2}\right] \frac{P_n\left(\boldsymbol{\xi}, \nu_o\right)}{\mathcal{J}},$$
$$\mathbf{V}_{j+2} = \sqrt{\xi_{j+1}\, \xi_{j+2}}\, P_n\left(\boldsymbol{\xi}, \nu_o\right) \boldsymbol{\Lambda}_{j+2}(\boldsymbol{r}), \quad \boldsymbol{\nabla} \cdot \mathbf{V}_{j+2} = \sqrt{\frac{\xi_{j+1}}{\xi_{j+2}}} \left[\frac{3\xi_{j+2} - 1}{2} + (2n + \nu_o) \frac{\left(\xi_{j+2} - 1\right) \xi_{j+2}^2}{\xi_{j+1}^2 + \xi_{j+2}^2}\right] \frac{P_n\left(\boldsymbol{\xi}, \nu_o\right)}{\mathcal{J}}$$</td></tr>
<tr><td colspan="2">The functions are defined on three adjacent quadrilateral cells locally numbered counterclockwise from 1 to 3. They are written using the zeroth-order vector functions $\boldsymbol{\Lambda}_\beta$ (which in turn depend on the edge-vectors $\boldsymbol{\ell}_\beta$ for $\beta = 1, 2, 3$, or 4), and the *scalar* functions P_n, $\mathcal{T}_n$, and $\mathcal{R}_n$, with $\mathcal{T}_n(1,1) = \mathcal{R}_n(1,1) = 0$, and
$$\boldsymbol{\Lambda}_\beta(\boldsymbol{r}) = \frac{\xi_{\beta+2} \boldsymbol{\ell}_{\beta-1}}{\mathcal{J}}, \qquad P_n\left(\boldsymbol{\xi}, \nu_o\right) = \sqrt{\left(\xi_{j+1}^2 + \xi_{j+2}^2\right)^{2n+\nu_o}},$$
$$\boldsymbol{\nabla} \cdot \boldsymbol{\Lambda}_\beta = \frac{1}{\mathcal{J}}, \qquad \mathcal{T}_n\left(\xi_a, \xi_b\right) = \frac{\sqrt{\left(\xi_a^2 + \xi_b^2\right)^{2n-1+\nu_o}}}{2\sqrt{\xi_a \xi_b}} \left[1 + (2n - 1 + \nu_o) \frac{2\, \xi_a^2}{\xi_a^2 + \xi_b^2}\right] - K_T,$$
$$\boldsymbol{\nabla} \xi_\beta \cdot \boldsymbol{\Lambda}_{\beta \pm 1} = 0, \qquad \mathcal{R}_n\left(\xi_a, \xi_b\right) = \frac{\sqrt{\left(\xi_a^2 + \xi_b^2\right)^{2n+\nu_e}}}{\sqrt{\xi_a \xi_b}} - K_R$$
The expressions reported in the Table are based on the assumption that the singular edge of cell 1 and 3 is along the $\xi_i = 0$ coordinate-line, and cell 2 has singular vertex in $\xi_{j+1} = \xi_{j+2} = 0$. $\boldsymbol{T}$ and $\boldsymbol{R}$ vanish at the vertex of cell 2 opposite the singular vertex by setting
$$K_T = \frac{\sqrt{2^{2n-1+\nu_o}}}{2} (2n + \nu_o), \; K_R = \sqrt{2^{2n+\nu_e}}$$</td></tr>
</table>

$\left\{\xi_j, \xi_{j\pm1}, \xi_{j+2}\right\}$. Cell 2 has its vertex $\xi_{j+1} = \xi_{j+2} = 0$ on the sector tip, while the singular edges of cells 1 and 3 are along the local coordinate-line $\xi_i = 0$, as in [3]. Fig. 3 shows the edge vectors $\boldsymbol{\ell}_{j+1}$ and $\boldsymbol{\ell}_{j+2}$ of cell 2, and the edge-vector $\boldsymbol{\ell}_i$ of the cells 1 and 3.

IV. BASIS FUNCTIONS FOR TIP SINGULARITIES

Table II shows the expression of the tip singular functions of singularity order n. $\boldsymbol{T}$ and $\mathbf{V}$ are tangential functions, $\boldsymbol{R}$ is an even radial function. The functions $\boldsymbol{T}$ and $\boldsymbol{R}$ are piecewise defined on three adjacent cells locally numbered counterclockwise from 1 to 3, as shown in Fig. 3. $\mathbf{V}_{j+1}$, $\mathbf{V}_{j+2}$ are bubble tangential functions that span only the number 2 cell. In the Table, $\mathcal{J}$ (with no subscript) indicates the Jacobian of the transformation from parent to child space of each cell. Demonstration of the continuity of the normal component of $\boldsymbol{T}$ and $\boldsymbol{R}$ along the edge in common to a cell pair is straightforward, and it is left to the interested reader. The value of the two constants K_T and K_R of Table II does not affect the conformity to the divergence of the functions and therefore, in applications, one can safely use $K_T = K_R = 0$.

By replacing $T_n(\xi_i, 1)$ with $(\nu \xi_i^{\nu-1} - 1)$ in the $\boldsymbol{T}_1$ and $\boldsymbol{T}_3$ parts of $\boldsymbol{T}$ on cells 1 and 3, one obtains the edge-singular functions

$$ {}^{e}\boldsymbol{\Lambda}_{i\pm1}(\boldsymbol{r}) = \left(\nu \xi_i^{\nu-1} - 1\right) \boldsymbol{\Lambda}_{i\pm1}(\boldsymbol{r}) \tag{9}$$

of [3, Table I], apart a sign adjustment. The same applies to functions $\boldsymbol{R}_1$ and $\boldsymbol{R}_3$.

The piece $\boldsymbol{T}_2$ of $\boldsymbol{T}$ has zero divergence and is obtained from the potential Φ_2 as follows:

$$\Phi_2 = \sqrt{\xi_{i+1}\, \xi_{i+2} \left(\xi_{i+1}^2 + \xi_{i+2}^2\right)^{\nu_o + 2n - 1}} \tag{10}$$

$$\boldsymbol{T}_2 = \hat{\boldsymbol{n}} \times \nabla \Phi_2 + K_T \left[\boldsymbol{\Lambda}_{j-1}(\boldsymbol{r}) - \boldsymbol{\Lambda}_j(\boldsymbol{r})\right] \tag{11}$$

where $\hat{\boldsymbol{n}}$ is the unit normal to the plane angular sector. Fig. 4 shows the behavior of $\boldsymbol{T}$ and $\boldsymbol{R}$ for $n = 0$ and $K_T = K_R = 0$ on a 90° sector described by three equal square cells of unit side. Fig. 5 shows the behavior of the bubble functions $\mathbf{V}_{j+1}$ and $\mathbf{V}_{j+2}$ for $n = 0$ on the same 90° sector.

Outside a small circular area around the tip, the normal component of the tip functions along the $\xi_{j+1} = 0$ edge (and the $\xi_{j+2} = 0$ edge) must go to zero as the square root of the distance from the edge itself [27], therefore proportional to $\sqrt{\xi_{j+1}}$ (or $\sqrt{\xi_{j+2}}$). Since the functions we consider are even or odd, the behavior is shown only for the components

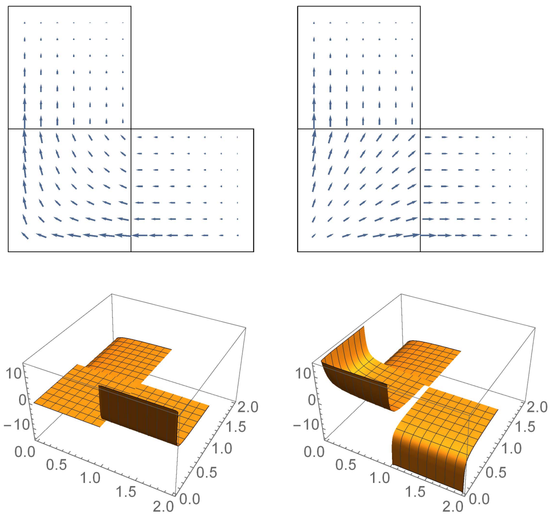

Fig. 4. Tip functions of singularity order $n = 0$ with vector plots reported at the top and divergence reported at the bottom. The behavior of the tangential function obtained for $\nu_o = 0.81466$ is shown at left. The radial function for $\nu_e = 0.29658$ is shown at right.

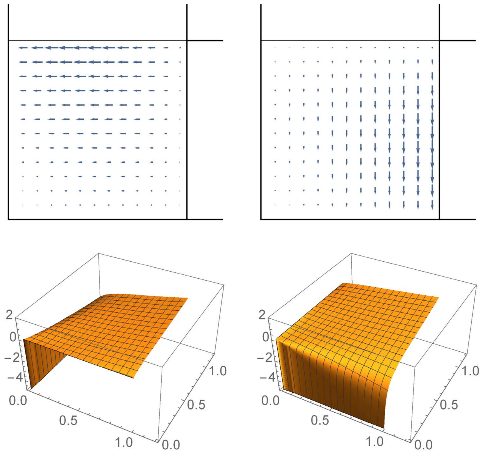

Fig. 5. Bubble functions $\mathbf{V}_{j+1}$ (at left) and $\mathbf{V}_{j+2}$ (at right) for $n = 0$, $\nu_o = 0.81466$. The vector function plots are at the top, their divergence is reported at the bottom. The divergence of $\mathbf{V}_{j+1}$ is zero along the $\xi_{j+2} = 0$ edge while $\nabla \cdot \mathbf{V}_{j+2} = 0$ along the $\xi_{j+1} = 0$ edge.

orthogonal to the $\xi_{j+1} = 0$ edge, that is, the components along the gradient of ξ_{j+1}. In fact, in the limit of small ξ_{j+1}, and for $0 \leq \xi_{j+1} < \xi_{j+2}$ and $K_T = K_R = 0$, one obtains

$$\begin{bmatrix} \boldsymbol{T}_2 \\ \boldsymbol{R}_2 \\ \mathbf{V}_{j+1} \end{bmatrix} \cdot \nabla \xi_{j+1} \approx \frac{\sqrt{\xi_{j+1}}}{\mathcal{J}} \begin{bmatrix} A_T\, \xi_{j+2}^{2n+\nu_o-3/2} \\ \xi_{j+2}^{2n+\nu_e-1/2} \\ -\xi_{j+2}^{2n+\nu_o+1/2} \end{bmatrix} \tag{12}$$

with $A_T = -(2\,n + \nu_o - 1/2)$.

TABLE III

TIP FUNCTIONS FOR A 90° CORNER

Odd functions
$\boldsymbol{T}_2 = \left[\frac{\rho^{\nu_o+2n-1}}{\sqrt{\sin(2\phi)}} + \mathrm{O}(\rho)\right]\left[\frac{\hat{\boldsymbol{\phi}}\,\sin(2\phi)(\nu_0+2n) - \hat{\boldsymbol{\rho}}\,\cos(2\phi)}{\sqrt{2}}\right]$
$\mathbf{V}_{\substack{j+1\\j+2}} = \sqrt{\frac{\sin(2\phi)}{2}}\,\rho^{\nu_o+2n+1}\left(\hat{\boldsymbol{\phi}}\begin{smallmatrix}\sin\phi\\\cos\phi\end{smallmatrix} \mp \hat{\boldsymbol{\rho}}\begin{smallmatrix}\cos\phi\\\sin\phi\end{smallmatrix}\right)[1+\mathrm{O}(\rho)]$
$\boldsymbol{\nabla}\cdot\boldsymbol{T}_2 = 0$
$\boldsymbol{\nabla}\cdot\mathbf{V}_{\substack{j+1\\j+2}} = \mp\frac{\rho^{\nu_o+2n}}{\sqrt{\sin(2\phi)}}\left\{\frac{1+(\nu_o+2n)[1\pm\cos(2\phi)]}{\sqrt{2}}\right\}\begin{smallmatrix}\sin\phi\\\cos\phi\end{smallmatrix}$ $+\sqrt{\sin(2\phi)}\;\mathrm{O}\left(\rho^{\nu_o+2n+1}\right)$
Even functions
$\boldsymbol{R}_2 = \left[\frac{\sqrt{2}\,\rho^{\nu_e+2n}}{\sqrt{\sin(2\phi)}} + \mathrm{O}(\rho)\right]\hat{\boldsymbol{\rho}}$
$\boldsymbol{\nabla}\cdot\boldsymbol{R}_2 = \frac{\sqrt{2}\,\rho^{\nu_e+2n-1}}{\sqrt{\sin(2\phi)}}(\nu_e+2n+1)+\mathrm{O}(1)$

O() is the Landau (big-O) symbol. Cell 2 has singular vertex at $\rho = 0$.

TABLE IV

PARENT TO POLAR COORDINATE MAPPING FOR THE UNIT RIGHT ANGLED CORNER CELL

$\hat{\boldsymbol{\rho}} = +\frac{(\xi_{j+1}\,\boldsymbol{\ell}_{j+2} - \xi_{j+2}\,\boldsymbol{\ell}_{j+1})}{\sqrt{\xi_{j+1}^2+\xi_{j+2}^2}}$ $\hat{\boldsymbol{\phi}} = -\frac{(\xi_{j+1}\,\boldsymbol{\ell}_{j+1} + \xi_{j+2}\,\boldsymbol{\ell}_{j+2})}{\sqrt{\xi_{j+1}^2+\xi_{j+2}^2}}$ $\boldsymbol{\ell}_{j+1} = -\left(\sin\phi\,\hat{\boldsymbol{\rho}} + \cos\phi\,\hat{\boldsymbol{\phi}}\right)$ $\boldsymbol{\ell}_{j+2} = +\left(\cos\phi\,\hat{\boldsymbol{\rho}} - \sin\phi\,\hat{\boldsymbol{\phi}}\right)$		
$\rho = \sqrt{\xi_{j+1}^2+\xi_{j+2}^2}$	$\cos\phi = \frac{\xi_{j+1}}{\sqrt{\xi_{j+1}^2+\xi_{j+2}^2}}$	$\sin\phi = \frac{\xi_{j+2}}{\sqrt{\xi_{j+1}^2+\xi_{j+2}^2}}$

Parent to polar coordinate mapping for a 90° corner valid for a square cell of unitary side length ($|\boldsymbol{\ell}_{j+2}| = |\boldsymbol{\ell}_{j+1}|$) and unitary Jacobian $\mathcal{J}$. The local polar reference frame (ρ, ϕ) is centered at the corner tip.

Table III clarifies the modeling capabilities of the tip functions on a 90° corner-cell with unitary Jacobian and side length. In this case, by introducing a local polar reference frame (ρ, ϕ) centered on the 90° tip, the tangential functions $\boldsymbol{T}_2$ and $\boldsymbol{R}_2$, and the bubble functions $\mathbf{V}$ simplify as in Table III, in agreement with Andersson [5] for $n = 0$, and with $\cos\phi$ and $\sin\phi$ given as in Table IV. Also, by considering the variation in ρ of these functions it is quite evident that, in the vicinity of the tip, these are in full agreement with the asymptotic expressions (1)–(3). Sufficiently far away from the tip and from the edge(s) opposite the tip, however, the singularity goes progressively over to the "edge" type. The $\boldsymbol{T}$, $\boldsymbol{R}$, and $\mathbf{V}$ functions can be normalized, for example, by setting

$$\iint_{\mathrm{cell2}} \sqrt{\boldsymbol{T}(n)\cdot\boldsymbol{T}(n)}\,\mathcal{J}\,\mathrm{d}\xi = 1 \tag{13}$$

$$\iint_{\mathrm{cell2}} \sqrt{\boldsymbol{R}(n)\cdot\boldsymbol{R}(n)}\,\mathcal{J}\,\mathrm{d}\xi = 1 \tag{14}$$

$$\iint_{\mathrm{cell2}} \sqrt{\mathbf{V}_{j+1}(n)\cdot\mathbf{V}_{j+1}(n)}\,\mathcal{J}\,\mathrm{d}\xi = 1 \tag{15}$$

$$\iint_{\mathrm{cell2}} \sqrt{\mathbf{V}_{j+2}(n)\cdot\mathbf{V}_{j+2}(n)}\,\mathcal{J}\,\mathrm{d}\xi = 1. \tag{16}$$

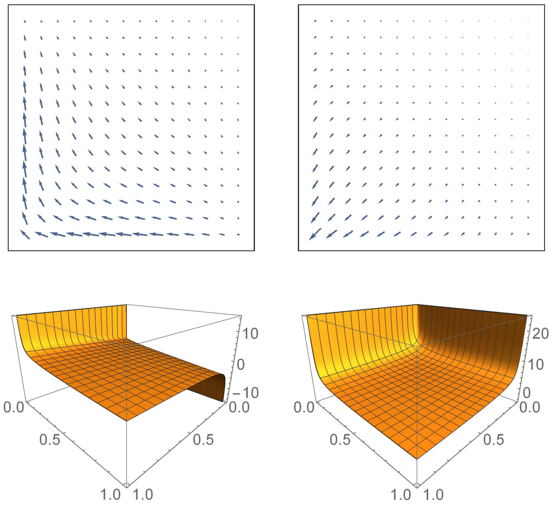

Fig. 6. Modified tip-functions $\widetilde{\boldsymbol{T}}$ and $\widetilde{\boldsymbol{R}}$ of singularity order $n = 0$ with vector plots reported at top and divergence reported at the bottom. The behavior of the tangential function obtained for $\nu_o = 0.81466$ is shown at left. The radial function for $\nu_e = 0.29658$ is shown at right.

As can be seen from Table III, the order $m = 2n - 1$ of the $\boldsymbol{T}$ function is lower than the order $m = 2n + 1$ of the bubble functions $\boldsymbol{\mathsf{V}}$. Therefore, $\boldsymbol{\mathsf{V}}$ functions of order n should only be used with the $\boldsymbol{T}$ function of order $n+1$. At this point, it is apparent that the bubble functions $\boldsymbol{\mathsf{V}}$ do not contribute to the currents near the tip. Thus, in applications it may be sufficient to use only the $\boldsymbol{T}$ and $\boldsymbol{R}$ functions of order $n = 0$. As a matter of fact, the $\boldsymbol{\mathsf{V}}$ bubble functions were introduced and discussed only to highlight that the function family of Table II models the asymptotic behavior of the current given in (1)–(3). A user may instead decide to use additional functions in the q series higher than order $q = 1$. However, it may be quite challenging to use functions of order $q > 1$ in an MoM code because these functions are not very linearly independent of each other. Given that as q grows the functions are essentially zero near the tip ($\rho = 0$), the singular tip behavior is primarily provided by the functions obtained with $q = 1$ (and $n = 0$).

V. MODIFICATION OF $\boldsymbol{T}$ AND $\boldsymbol{R}$ INTO BUBBLE FUNCTIONS

The divergence-conforming $\boldsymbol{T}$ and $\boldsymbol{R}$ functions of Section IV span three cells; cell 2 containing the tip and adjacent cells 1 and 3. However, it is simple to modify these functions so that they span only cell 2 by adding some corrective terms to $\boldsymbol{T}_2$ and $\boldsymbol{R}_2$ that make them vanish along the edges in common with cells 1 and 3. The corrective terms shall not modify the value of the function and its divergence at the tip. In this way, one obtains functions of the type shown in Fig. 6 (we suggest the reader compare this figure with Fig. 4).

For example, the $\boldsymbol{T}_2$ function of Table II obtained for $K_T = 0$ can be modified to obtain the tangential function

$$\begin{aligned}\widetilde{\boldsymbol{T}} &= \boldsymbol{T}_2 + \xi_{j+1}\,\mathcal{T}_n\big(\xi_{j+2},1\big)\,\boldsymbol{\Lambda}_{j-1}(\boldsymbol{r})\\ &\quad - \xi_{j+2}\,\mathcal{T}_n\big(\xi_{j+1},1\big)\,\boldsymbol{\Lambda}_{j}(\boldsymbol{r}) \qquad (17)\\ \nabla\cdot\widetilde{\boldsymbol{T}} &= \frac{\xi_{j+1}\,\mathcal{DT}_n\big(\xi_{j+2}\big) - \xi_{j+2}\,\mathcal{DT}_n\big(\xi_{j+1}\big)}{\mathcal{J}} \qquad (18)\end{aligned}$$

with

$$\mathcal{T}_n(\xi_a,1) = \left[\frac{1}{2} + \frac{\xi_a^2(2n-1+\nu_o)}{\xi_a^2+1}\right]\frac{\sqrt{\left(\xi_a^2+1\right)^{2n-1+\nu_o}}}{\sqrt{\xi_a}} \qquad (19)$$

$$\mathcal{DT}_n(\xi_a) = \left[1+\xi_a^2(2\nu_o+4n-1)\right]\frac{\sqrt{\left(\xi_a^2+1\right)^{2n-3+\nu_o}}}{\sqrt{\xi_a}}. \qquad (20)$$

The divergence of $\widetilde{\boldsymbol{T}}$ is no longer zero but vanishes at the tip.

Likewise, one can add a corrective term to the $\boldsymbol{R}_2$ function of Table II obtained for $K_R = 0$ to produce the radial function

$$\begin{aligned}\widetilde{\boldsymbol{R}} &= \boldsymbol{R}_2 - \xi_{j+1}\,\mathcal{R}_n\big(\xi_{j+2},1\big)\,\boldsymbol{\Lambda}_{j-1}(\boldsymbol{r})\\ &\quad - \xi_{j+2}\,\mathcal{R}_n\big(\xi_{j+1},1\big)\,\boldsymbol{\Lambda}_{j}(\boldsymbol{r})\\ &\quad + \frac{1-\xi_{j+1}^2}{\sqrt{\xi_{j+2}}}\frac{\boldsymbol{\ell}_j}{\mathcal{J}} - \frac{1-\xi_{j+2}^2}{\sqrt{\xi_{j+1}}}\frac{\boldsymbol{\ell}_{j-1}}{\mathcal{J}} \qquad (21)\\ \mathcal{J}\,\nabla\cdot\widetilde{\boldsymbol{R}} &= (2n+1+\nu_e)\,\mathcal{R}_n\big(\xi_{j+1},\xi_{j+2}\big)\\ &\quad - 2\big[\xi_{j+1}\,\mathcal{R}_n\big(\xi_{j+2},1\big) + \xi_{j+2}\,\mathcal{R}_n\big(\xi_{j+1},1\big)\big]\\ &\quad + 2\left(\frac{\xi_{j+1}}{\sqrt{\xi_{j+2}}} + \frac{\xi_{j+2}}{\sqrt{\xi_{j+1}}}\right) \qquad (22)\end{aligned}$$

with

$$\mathcal{R}_n(\xi_a,\xi_b) = \frac{\sqrt{\left(\xi_a^2+\xi_b^2\right)^{2n+\nu_e}}}{\sqrt{\xi_a\xi_b}}. \qquad (23)$$

The last two terms on the right-hand side of (21) ensure that the divergence does not change sign along the two edges that form the tip. The modified tip functions $\widetilde{\boldsymbol{T}}$ and $\widetilde{\boldsymbol{R}}$ of singularity order $n = 0$ are shown in Fig. 6.

The preceding equations constitute an additive correction technique, but alternatively one can use a multiplicative correction technique to replace $\boldsymbol{T}_2$ and $\boldsymbol{R}_2$ with

$$\widetilde{\boldsymbol{T}} = \boldsymbol{T}_2\,\cos^2\!\left(\frac{\pi\xi_{j+1}}{2}\right)\cos^2\!\left(\frac{\pi\xi_{j+2}}{2}\right) \qquad (24)$$

$$\widetilde{\boldsymbol{R}} = \boldsymbol{R}_2\,\cos^2\!\left(\frac{\pi\xi_{j+1}}{2}\right)\cos^2\!\left(\frac{\pi\xi_{j+2}}{2}\right). \qquad (25)$$

The divergence of (24) and (25) is

$$\begin{aligned}\nabla\cdot\widetilde{\boldsymbol{T}} &= \pi\,\frac{\sqrt{\left(\xi_{j+1}^2+\xi_{j+2}^2\right)^{2n-3+\nu_o}}}{4\,\mathcal{J}\sqrt{\xi_{j+1}\xi_{j+2}}}\\ &\quad \left[\left(\xi_{j+1}^2-\xi_{j+2}^2\right)A - 2\xi_{j+1}\xi_{j+2}(2n+\nu_o)B\right] \qquad (26)\end{aligned}$$

$$\begin{aligned}\nabla\cdot\widetilde{\boldsymbol{R}} &= -\frac{\sqrt{\left(\xi_{j+1}^2+\xi_{j+2}^2\right)^{2n+\nu_e}}}{\mathcal{J}\sqrt{\xi_{j+1}\xi_{j+2}}}\\ &\quad \times\left[\pi\frac{A}{2} - (2n+1+\nu_e)\cos^2\!\left(\frac{\pi\xi_{j+1}}{2}\right)\right.\\ &\quad \left.\cos^2\!\left(\frac{\pi\xi_{j+2}}{2}\right)\right] \qquad (27)\end{aligned}$$

with

$$\begin{aligned}A &= \xi_{j+1}\sin(\pi\xi_{j+1})\cos^2\!\left(\frac{\pi\xi_{j+2}}{2}\right)\\ &\quad + \xi_{j+2}\sin(\pi\xi_{j+2})\cos^2\!\left(\frac{\pi\xi_{j+1}}{2}\right) \qquad (28)\end{aligned}$$

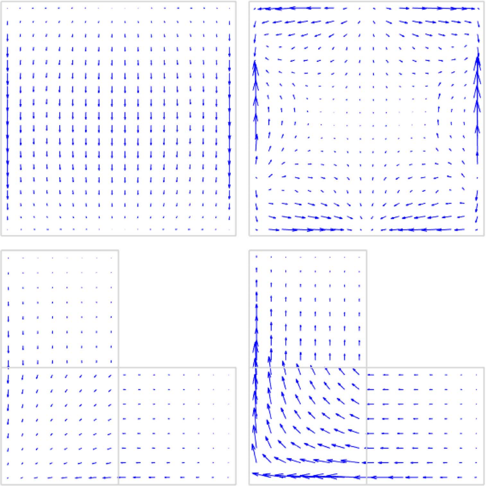

Fig. 7. Real part of the current induced on a $1\lambda \times 1\lambda$ plate at normal incidence. The results at top-left are obtained with the $[p, s, m] = [1, 1, 0]$ base. The upper-right figure shows the difference in the real current obtained with and without the tip-singular bases, magnified by a factor of 10. The bottom figures show the contributions of the even (left) and odd (right) tip-singular functions to the upper-left result, magnified by a factor of 20.

$$B = \xi_{j+1} \sin(\pi \xi_{j+2}) \cos^2\left(\frac{\pi \xi_{j+1}}{2}\right) - \xi_{j+2} \sin(\pi \xi_{j+1}) \cos^2\left(\frac{\pi \xi_{j+2}}{2}\right). \tag{29}$$

Once again, the last two terms on the right-hand side of (21) should be added to (25) to guarantee that the divergence of $\widetilde{\boldsymbol{R}}$ does not change sign along the two edges that form the tip. We leave as an exercise for the interested reader to derive the analytical expression for the divergence of these latter functions.

VI. NUMERICAL RESULTS

This section reports results for infinitely thin metal plates obtained by solving the EFIE with and without the tip-singular functions presented in this article; the representation includes the edge-singular quadrilateral basis of order $[p, s, m]$ illustrated in [3]. The edge-singular background base is described by an integer p denoting the background polynomial order, an integer s giving the number of fractional exponents from [3, eq. (4)] included in the edge-singular representation, and an integer m providing the order of the edge-singular basis subset in the longitudinal direction. For the tip-singular functions, we report results obtained as follows.

1) The tip-functions described in Section IV that span three rectangular cells (tip-functions A).
2) The multiplicative corrected tip-functions given in (24) and (25) that span only the cell at the corner (tip-functions B).

Fig. 7 shows results for the current induced by a monochromatic plane wave normally incident on a square plate of size $1\lambda \times 1\lambda$ meshed with 25 square cells of equal size $\lambda/5 \times \lambda/5$. The plate is in the x, y-plane with sides parallel to x and y, and the incident E-field is polarized in the negative $\hat{\boldsymbol{y}}$-direction. The figure shows results only for the real part of the current; the imaginary part which is smaller than the real part is not reported. Fig. 7 at top left was obtained by augmenting the [1,1,0] base with tip-singular basis functions of the A type. Fig. 7 at top right show the difference between the results at top left and the results obtained with the standard [1,1,0] base without tip-singular basis functions (magnified by a factor of 10). The contribution to the current shown at top-left given just by the tip-singular even (at left) and odd (at right) functions is shown in the bottom part of the figure. Since we have used type A tip-functions, these contributions span only the three square cells that form each of the four plate corners, and not the entire plate; the figures at bottom show only the behavior around the bottom left corner of the plate.

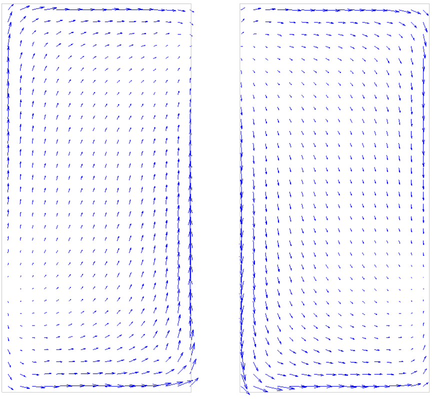

Fig. 8. Imaginary part of the induced current at grazing incidence on two plates $0.2\lambda \times 0.4\lambda$ spaced 0.05λ obtained using the [1,1,0] order base augmented with the type B tip-singular functions.

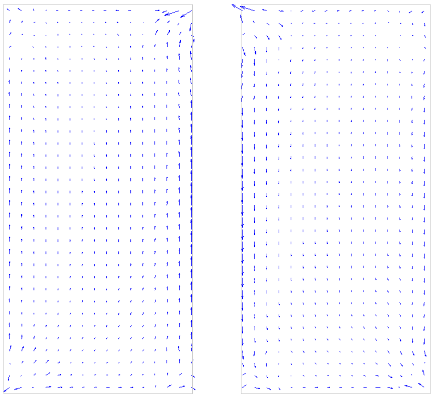

Fig. 9. Imaginary part of the difference between results obtained with and without tip-singular functions, magnified by a factor of 20.

For the far-zone fields, the results with and without the tip-singular functions are similar. Nonetheless, near-field differences in the current density are clearly visible in Fig. 7 at top right. The order of the system matrix of the problem treated with the edge-singular base of [3] (without the tip functions) is 216, with CN = 440. With the tip functions, the order of the system matrix is 224, with CN = 600.

Figs. 8 and 9 consider the case of two $0.2\lambda \times 0.4\lambda$ plates located in the Cartesian plane x, y with sides parallel to x and y, and separated by a gap of 0.05λ. Each plate is meshed identically by using 32 square cells of sidelength

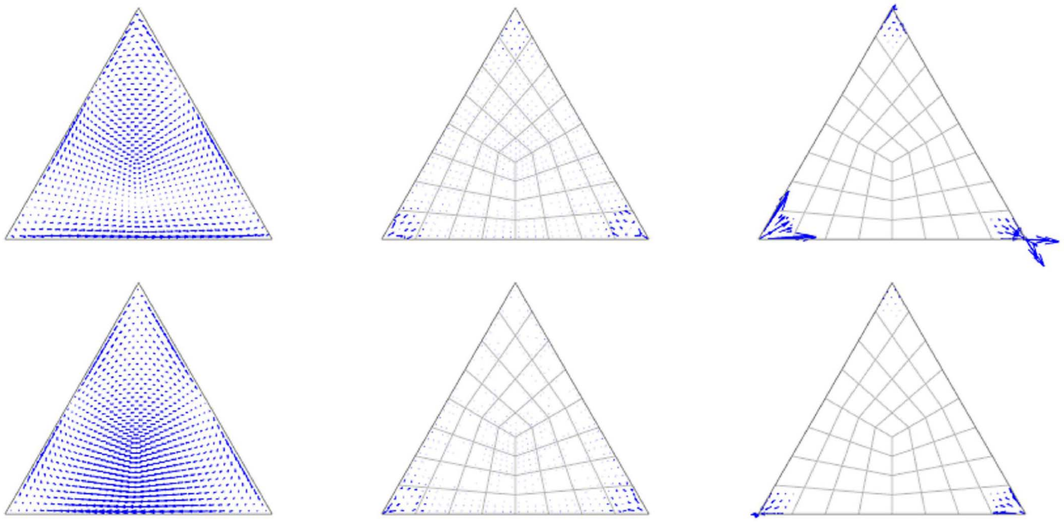

Fig. 10. Equilateral triangular plate at grazing incidence. The lefthand column of the figure shows, with the same scale, the real (at top) and imaginary (at bottom) parts of the induced current obtained with the [1,1,0] base augmented by the tip-basis functions of the B type. The central column shows the difference between the current obtained with and without the tip-singular functions, magnified by a factor of 10. At right, we show the contribution due just to the tip-singular functions, also scaled by 10×. The 48-cell mesh is shown in the figures in the central and righthand columns.

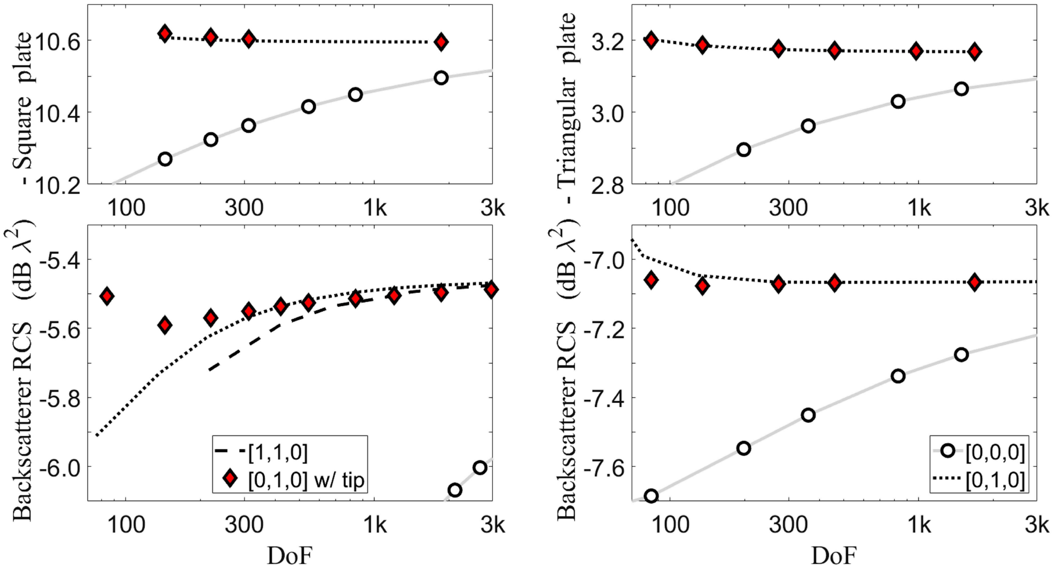

Fig. 11. Backscatterer RCS versus the total number of unknowns (DoF) for the $1\lambda \times 1\lambda$ square plate (left-hand column), and for the equilateral triangular plate with sides equal to 1λ (right-hand column), as the quadrilateral-cell meshes are uniformly refined. The results are reported using the same vertical scale in dB square wavelengths; normal incidence results are reported at top, grazing incidence results at bottom. The legends of the bottom figures show the markers used to distinguish the results obtained with four different base orders. Results for the [1,1,0] base are shown only in the figure at the bottom left since they overlap the results obtained with the base [0,1,0] in the other figures. The results marked with red diamonds are obtained with a base augmented by the tip-singular functions B.

$\lambda/20$. The plates are illuminated by a grazing-incident plane wave propagating along the positive $\hat{\boldsymbol{y}}$-axis with a unitary E-field polarized along the positive $\hat{\boldsymbol{x}}$-direction. This structure has been studied numerically by using the [1,1,0] order base augmented or not with the type B tip-singular functions. While the real part of the induced current shows little difference after incorporating the tip-functions, some differences are evident in the imaginary component of the induced current shown in Fig. 8.

Fig. 9 shows the difference in the imaginary currents of the two-plate problem of Fig. 8 obtained with and without the tip-singular functions, magnified by a factor of 20. It is evident that the dominant difference is due to the radial (even) component of the current at the two adjacent tips along the trailing edges (top of figure) of the plates.

Quadrilateral cells can model tips for a fairly wide range of salient angles; for example, let us consider the triangular plate of Fig. 10 located in the first quadrant of the Cartesian plane x, y, with a side parallel to the x-axis, and on which impinges a grazing plane-wave propagating along the positive $\hat{\boldsymbol{y}}$-axis with unitary E-field polarized along the positive $\hat{\boldsymbol{x}}$-direction. Fig. 10 shows the real (top row) and the imaginary part (bottom row) of the current on the triangular plate (with sides equal to 1λ) obtained with the [1,1,0] base augmented by the tip-basis functions of the B type. Exponents for a 60° corner are $\nu_o = 0.91904$ and $\nu_e = 0.24010$. It appears that in this case the even tip singularity prevails over the odd one for the two corners at bottom; for the top corner it is the other way around.

The preceding plots show differences between the results obtained with and without the tip singular functions in the near-field region (for example, for the induced currents), but differences can also be observed for far-field results. Fig. 11 shows the backscatterer radar-cross section (RCS) obtained with bases of different orders for the square plate of size $1\lambda \times 1\lambda$ considered in Fig. 7 (left-hand column), and for the equilateral triangular plate with sides equal to 1λ of Fig. 10 (right-hand column). Normal incidence results are reported at top, grazing incidence results are given at bottom. The results obtained with a base augmented by the tip singular functions B are those marked with the red diamonds. From these results, it is quite evident that relative to a pure polynomial representation, the edge-singular functions dramatically improve the convergence of these results, while the tip-singular functions provide a more minor, secondary level of improvement that is more noticeable for grazing incidence than for normal incidence.

VII. CONCLUSION

New families of divergence-conforming basis functions for modeling the singularities associated with current and charge density at tips are presented. The new basis functions are used to increment existing edge-singular bases so that on cells that contain a singular tip where two singular edges join together, the final base combines a hierarchical polynomial representation with linearly independent singular terms that incorporate general exponents that may be adjusted for the specific wedge angle of interest along edges and for the specific corner angle at the tip. Results for the current induced by plane waves incident on infinitely thin rectangular or triangular plates are presented. From the few test cases examined in this article, all of which involved problems where large edge currents were induced by the excitations, one may conclude that the addition of tip-singular functions to the existing edge-singular basis sets generally provides second-order improvements in the numerical results. In situations where edge effects are less pronounced, however, tip singularities may take on greater importance.

REFERENCES

[1] R. D. Graglia and A. F. Peterson, *Higher-order Techniques in Computational Electromagnetics*. Rijeka, Croatia: SciTech, 2016.

[2] R. D. Graglia and G. Lombardi, "Singular higher order divergence-conforming bases of additive kind and moments method applications to 3D sharp-wedge structures," *IEEE Trans. Antennas Propag.*, vol. 56, no. 12, pp. 3768–3788, Dec. 2008.

[3] R. D. Graglia, A. F. Peterson, and P. Petrini, "Hierarchical divergence conforming bases for edge singularities in quadrilateral cells," *IEEE Trans. Antennas Propag.*, vol. 66, no. 11, pp. 6191–6201, Nov. 2018, doi: 10.1109/TAP.2018.2854298.

[4] A. F. Peterson and R. D. Graglia, "Basis functions for vertex, edge, and corner singularities: A review," *IEEE J. Multiscale Multiphys. Comput. Techn.*, vol. 1, pp. 161–175, 2016.

[5] T. Andersson, "Moment-method calculations scattering by a square plate using singular basis functions multipole expansions," Dept. Electromagn. Theory, Lund Inst. Technol., Lund, Sweden, Tech. Rep. LUTEDX/(TEAT-7014)/1-28/(1991); vol. TEAT-7014, 1991.

[6] J. Van Bladel, *Singular Electromagnetic Fields and Sources*. Oxford, U.K.: Clarendon, 1991.

[7] R. S. Satterwhite and R. G. Kouyoumjian, "Electromagnetic diffraction by a perfectly-conducting plane angular section," Ohio State Univ., Columbus, OH, USA, Tech. Rep. 2183-2, AFCRL-69-0401, 1970.

[8] R. De Smedt and J. G. Van Bladel, "Field singularities near aperture corners," *IEE Proc. A (Phys. Sci., Meas. Instrum., Manage. Educ., Rev.)*, vol. 134, no. 8, pp. 694–698, Sep. 1987.

[9] J. Boersma and J. K. M. Jansen, "Electromagnetic field singularities at the tip of an elliptic cone," Eindhoven Univ. Technol., Eindhoven, The Netherlands, Tech. Rep. 90-WSK-01, Dec. 1990.

[10] D. S. Jones, "Diffraction by an edge and by a corner," *Quart. J. Mech. Appl. Math.*, vol. 5, no. 3, pp. 363–378, 1952.

[11] L. Kraus, "Diffraction by a plane angular sector," Ph.D. dissertation, Graduate School Arts Sci., New York Univ., New York, NY, USA, 1955.

[12] W. Braunbek, "On the diffraction field near a plane-screen corner," *IRE Trans. Antennas Propag.*, vol. 4, no. 3, pp. 219–223, Jul. 1956.

[13] J. Radlow, "Diffraction by a quarter-plane," *Arch. for Rational Mech. Anal.*, vol. 8, no. 1, pp. 139–158, Jan. 1961.

[14] J. Radlow, "Note on the diffraction at a corner," *Arch. Ration. Mech. Anal.*, vol. 19, pp. 62–70, 1965.

[15] J. J. Bowman, T. B. A. Senior, and P. L. E. Uslenghi, Eds., *Electromagnetic and Acoustic Scattering by Simple Shapes*. New York, NY, USA: Hemisphere Pub.Co., 1969, ch. 18, pp. 637–701.

[16] R. S. Satterwhite, "Diffraction by a quarter plane, the exact solution, and some numerical results," *IEEE Trans. Antennas Propag.*, vol. 22, no. 3, pp. 500–503, May 1974.

[17] V. G. Daniele and G. Lombardi, "Wiener-hopf solution for impenetrable wedges at skew incidence," *IEEE Trans. Antennas Propag.*, vol. 54, no. 9, pp. 2472–2485, Sep. 2006.

[18] M. Albani, "On Radlow's quarter-plane diffraction solution," *Radio Sci.*, vol. 42, no. 6, pp. 1–10, Dec. 2007.

[19] V. Daniele and G. Lombardi, "On the scattering by a quarter-plane," in *Proc. Int. Conf. Electromagn. Adv. Appl.*, Sep. 2011, pp. 749–752.

[20] V. G. Daniele and R. S. Zich, *The Wiener-Hopf Method in Electromagnetics*. Rijeka, Croatia: SciTech, 2012.

[21] M. A. Lyalinov and N. Y. Zhu, *Scattering of Waves by Wedges and Cones with Impedance Boundary Conditions*. Rijeka, Croatia: SciTech, 2013.

[22] R. C. Assier and A. V. Shanin, "Diffraction by a quarter–plane. Analytical continuation of spectral functions," *Quart. J. Mech. Appl. Math.*, vol. 72, no. 1, pp. 51–86, 2019.

[23] T. J. Brinkley, "Current near the vertex of a perfectly conducting angular sector," Ph.D. dissertation, Dept. Elect. Eng., Ohio State Univ., Columbus, OH, USA, 1991.

[24] A. K. Ozturk, R. Paknys, and C. W. Trueman, "First-order singular basis functions for corner diffraction analysis using the method of moments," *IEEE Trans. Antennas Propag.*, vol. 57, no. 10, pp. 3160–3168, Oct. 2009.

[25] R. D. Graglia, P. Petrini, and A. F. Peterson, "Integral transformations to handle corner function singularities," *IEEE Trans. Antennas Propag.*, vol. 68, no. 12, pp. 7995–8008, Dec. 2020.

[26] R. D. Graglia, A. F. Peterson, and P. Petrini, "Computation of EFIE matrix entries with singular basis functions," *IEEE Trans. Antennas Propag.*, vol. 66, no. 11, pp. 6217–6224, Nov. 2018.

[27] D. R. Wilton, A. W. Glisson, and C. M. Butler, "Numerical solutions for scattering by rectangular bent plate structures," Dept. Elect. Eng., Univ. Mississippi, Oxford, MS, USA, Tech. Rep. N00123-75-C-1372, Oct. 1976.